NANO LETTERS

pubs.acs.org/NanoLett

Entropy-Driven Formation of Binary Semiconductor-Nanocrystal Superlattices

Wiel H. Evers,[†] Bart De Nijs,[‡] Laura Filion,[‡] Sonja Castillo,[†] Marjolein Dijkstra,[‡] and Daniel Vanmaekelbergh*,[†]

[†]Condensed Matter and Interfaces and [‡]Soft Condensed Matter, Debye Institute for NanoMaterials Science, University of Utrecht, Princetonplein 1, 3508 TA Utrecht, The Netherlands

ABSTRACT One of the main reasons for the current interest in colloidal nanocrystals is their propensity to form superlattices, systems in which (different) nanocrystals are in close contact in a well-ordered three-dimensional (3D) geometry resulting in novel material properties. However, the principles underlying the formation of binary nanocrystal superlattices are not well understood. Here, we present a study of the driving forces for the formation of binary nanocrystal superlattices by comparing the formed structures with full free energy calculations. The nature (metallic or semiconducting) and the size-ratio of the two nanocrystals are varied systematically. With semiconductor nanocrystals, self-organization at high temperature leads to superlattices (AlB_2, $NaZn_{13}$, $MgZn_2$) in accordance with the phase diagrams for binary hard-sphere mixtures; hence entropy increase is the dominant driving force. A slight change of the conditions results in structures that are energetically stabilized. This study provides rules for the rational design of 3D nanostructured binary semiconductors, materials with promises in thermoelectrics and photovoltaics and which cannot be reached by any other technology.

KEYWORDS Nanocrystals, self-assembly, superlattices, hard spheres, thermodynamics.

Colloidal, monolayer-stabilized nanocrystals (NC) can be synthesized with a nearly spherical shape and with a well-defined diameter that does not vary by more than 5% in the sample. Because of their monodisperse size and shape, such NCs show a strong propensity to assemble into NC superlattices.[1] More than a decade ago, the formation of single-component superlattices that consist of CdSe semiconductor NCs was reported.[1] This was followed by the demonstration of binary superlattices, consisting of NCs of different diameters and different nature, that is, semiconductor, metallic, or magnetic.[1−13] In such systems, novel collective properties can arise from the (quantum mechanical) interactions between the different components that are in close contact in a three-dimensional (3D) ordered geometry. Some striking examples have already been reported.[3,4,14,15] For instance, a binary superlattice of two types of insulator nanoparticles is found to become conductive due to interparticle charge transfer.[3] Colloidal crystallization is the only method known to date to obtain nanostructured systems with order in three dimensions. However, for further progress in the field of designed nanostructured materials, improved control of nanocolloid crystallization is a key factor.

Apart from the viewpoint of emerging nanomaterials, the formation of (binary) NC superlattices is of strong interest in colloidal science. Nanocrystals have a mass that is about a million times smaller than that of the colloidal particles commonly used in crystallization studies; hence, their thermal velocity is about a factor of thousand higher. This agrees with the fact that nanocolloid crystallization is a relatively fast process, still occurring under (near) equilibrium conditions. While crystallization of micrometer-sized colloids takes days to months,[16] NC superlattices are formed within a few minutes. Fast and reversible crystallization should allow one to study the thermodynamics of NC superlattice formation in a broad parameter range. Although a plethora of NC superlattices have been reported, the principles underlying their formation have not been studied systematically. For instance, attractions as well as entropic factors have been proposed as the driving force behind the formation of binary superlattices[10] but clear rules have not been presented.

In the case of micrometer-sized colloids, the interactions between the particles can be tailored and systems are available that resemble hard spheres.[16−21] It has been shown that the crystallization of a binary mixture of micrometer-sized colloidal hard spheres is driven only by an increase in entropy.[16,19,21] In the case of monolayer-stabilized NCs in a good organic solvent, the effective interaction consists to a first approximation of van der Waals attraction between the cores and steric repulsion between the stabilizing ligand molecules. The van der Waals attraction between two *semiconductor* nanocrystals is weak due to the large center-to-center distance between the NC cores, and is almost completely screened by the steric repulsion (see Supporting Information, Section III). Hence, semiconductor nanocrystals in a good solvent may have an interaction potential resembling that of hard spheres. In contrast, when metal nanocrystals are involved, the van der Waals attrac-

* To whom correspondence should be addressed. E-mail: d.vanmaekelbergh@uu.nl.
Received for review: 08/2/2010
Published on Web: 09/03/2010

© 2010 American Chemical Society

DOI: 10.1021/nl102705p | *Nano Lett.* **2010,** *10,* 4235–4241

tions are stronger and the pair potential exceeds the thermal energy considerably (Supporting Information, Section III).

Here, we present a systematic study of the thermodynamic driving force behind the formation of binary nanocrystal superlattices by comparing the crystal structures formed with phase diagrams obtained for binary mixtures of hard spheres, the free energy being calculated with the Frenkel-Ladd Einstein integration method in computer simulations (see Supporting Information). We have combined two different semiconductor NCs (i.e., PbSe and CdSe NC), as well as a semiconductor NC (PbSe) with metallic gold NCs. We have studied superlattice formation induced by the evaporation of the solvent, that is, by increasing the particle concentration at a controlled and variable temperature. Second, crystallization was initiated by increasing the interaction between the particles by addition of a nonsolvent. The NC size ratio and, in several cases, also the relative particle concentration (composition) in the binary suspensions were varied systematically. Solvent evaporation from mixtures of semiconductor NCs results in superlattices that agree to a large extent with the theoretical phase diagrams of binary hard-sphere mixtures, provided that the temperature is sufficiently high. This is in contrast with the formation of superlattices (i) at lower temperature, (ii) when metallic nanocrystals are involved, or (iii) when a nonsolvent is added to increase the interactions. In all these cases, superlattices that are known to be unstable for binary hard-sphere mixtures are formed, implying that van der Waals attractions become important.

We have studied the formation of superlattices starting from binary mixtures of PbSe and CdSe NCs, or PbSe and gold NCs. The effective diameter of the NCs was obtained from the center-to-center distance in transmission electron microscopy (TEM) pictures of the single-component face-centered-cubic (fcc) lattices. While we label our single-component lattices fcc, from our experimental data we cannot distinguish between fcc, hexagonal close-packed (hcp), and random stackings of hexagonal planes. In the first case, the effective diameter of the PbSe NCs was varied between 7 and 11 nm, while that of the CdSe NCs was 5.8 nm; hence, the size ratio γ ranged from 0.53 to 0.83. In binary mixtures of PbSe and Au NCs, γ varied between 0.47 and 0.86. The size dispersion in the original suspensions was $\leq$5% for the PbSe and CdSe suspensions and about 10% for the Au NC suspensions. Nanocolloid crystallization by solvent evaporation was achieved under controlled pressure ($\sim$10 mbar) and temperature (20 °C $\leq T \leq$ 70 °C). The TEM substrate was tilted over an angle of 30° with respect to the liquid/air interface. Previous studies have shown that crystal nucleation occurs at the organic liquid/air interface.[9] Generally, colloidal crystallization leads to a polycrystalline thin-film solid, with single-crystal domains between 1 and 10 μm in size. Examples are presented in Figures 1 and 3, and in Supporting Information. We have analyzed the crystal structures that are present on the TEM grids and measured the relative surface area that they occupy on the grid. In several cases, the relative importance of a given crystal structure depends on the particle concentration ratio in the binary suspension. Addition of a nonsolvent that increases the van der Waals attractions leads to the formation of 3D single-component superlattices that we collected by dipping a TEM grid in the suspension.

Phase Diagrams for Binary Hard-Sphere Mixtures. The self-assembled crystal structures on the TEM grids are compared with the phase diagrams as determined from free energy calculations using the Frenkel-Ladd Einstein thermodynamic integration in computer simulations for binary mixtures of hard spheres.[17−20] Using this method, the free-energy can be determined exactly and accounts for all entropic contributions. From the available theoretical predictions, the following conclusions can be drawn (Supporting Information, Section II): apart from the single-component fcc phases, for $0.414 \leq \gamma \leq 0.45$, NaCl is stable;[17] for $0.45 \leq \gamma \leq 0.61$, AlB_2 is stable;[17−19] for $0.54 \leq \gamma \leq 0.625$, $NaZn_{13}$ is stable;[18,19] and for $0.76 \leq \gamma \leq 0.84$ it was recently established that the Laves phases ($MgZn_2$, $MgCu_2$, $MgNi_2$) are stable,[20] although their maximum filling fraction is lower than that of the fcc lattice. Note that between $0.63 \leq \gamma \leq 0.75$ there are no known stable binary hard-sphere crystal structures.

Binary Crystal Structures Formed by Solvent Evaporation. The results obtained with the method of solvent evaporation are summarized in Tables 1 (combinations of PbSe and CdSe semiconductor NCs) and 2 (combinations of PbSe and Au NCs); see Supporting Information, Section I. For convenience, the results obtained with the solvent evaporation method will be presented here in order of increasing size ratio γ and according to the theoretically predicted stability regions for binary hard-sphere crystal structures.

In the range $0.45 < \gamma < 0.54$, we have performed several experiments. Combining the large PbSe and smaller Au NCs (Supporting Information, Table 2), we observed mostly single-component lattices of PbSe and Au NCs. Binary lattices covering small fractions (about 1%) of the TEM grid were observed occasionally. An overview of a TEM grid with details is shown in Supporting Information, Figure S1. In contrast, solvent evaporation from a binary suspension of two semiconductor NCs, that is, large PbSe and smaller CdSe NCs ($\gamma = 0.53$) at 70 °C, leads to superlattice films that contain $PbSe(CdSe)_2$ structures and the single-component fcc phases. The $PbSe(CdSe)_2$ superlattice is isostructural with AlB_2. Upon changing the particle concentration ratio of PbSe and CdSe NCs in the suspension, we found that the AlB_2 phases reach a maximum surface coverage of about 60% at a particle number concentration ratio of 10; this happens at the cost of the single-component phases (see Figure 2). We remark that the binary $PbSe(CdSe)_{13}$ crystal structure is also observed, however with a low surface coverage that does not increase with increasing the particle concentration

© 2010 American Chemical Society

DOI: 10.1021/nl102705p | Nano Lett. 2010, 10, 4235−4241

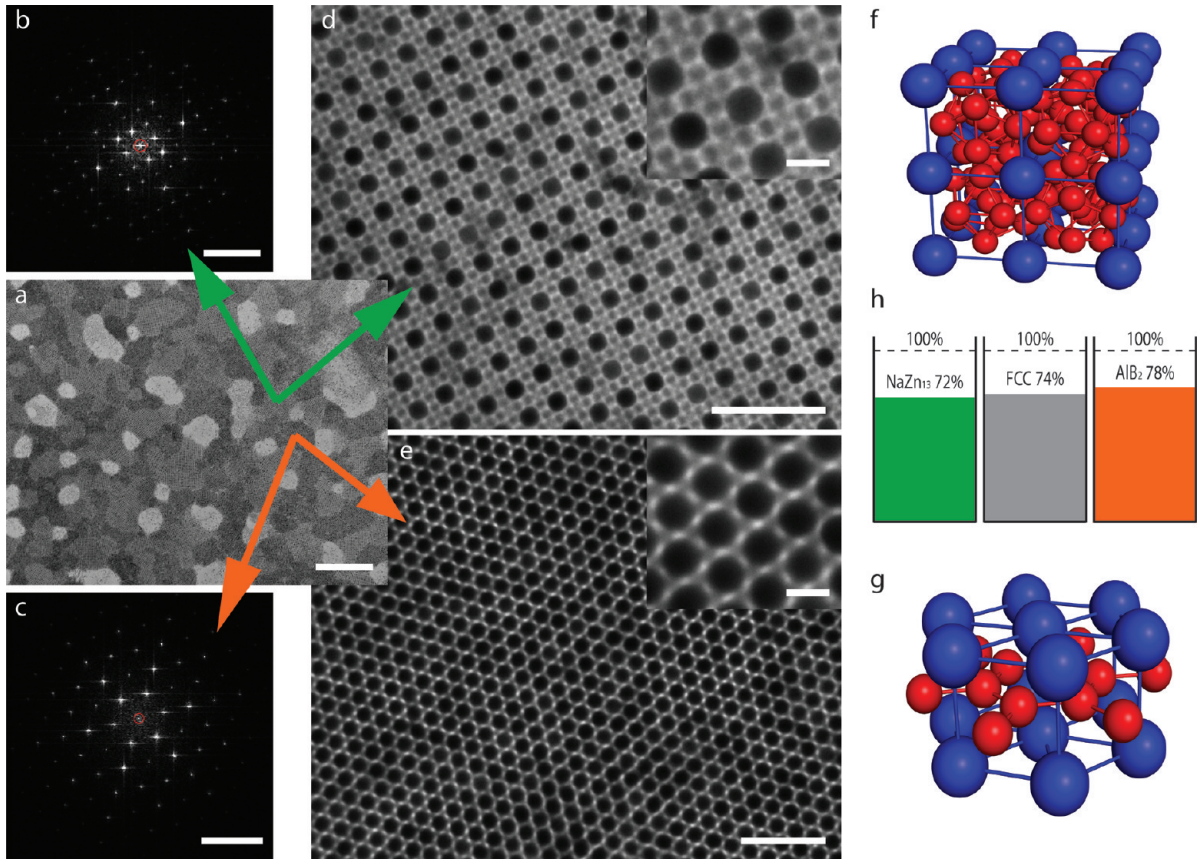

FIGURE 1. Binary superlattices obtained by solvent evaporation at 70 °C from a suspension of PbSe nanocrystals (11.0 nm effective diameter) and CdSe nanocrystals (5.8 nm effective diameter) at a size ratio γ of 0.53 and particle concentration ratio of about 4. (a) Overview of the TEM grid with different domains; (b,d,f) Fourier transform, TEM projection, and unit cell of a part of a PbSe(CdSe)13 domain; (c,e,g) Fourier transform, TEM projection, and unit cell of a part of a PbSe(CdSe)2 domain; (h) filling fractions of the observed binary lattices with respect to the fcc lattice. The scale bars are 500 nm for panel a, 0.25 nm^{-1} for panels b and c, 50 nm for panels d and e, and 10 nm for the insets of panel d and e.

of the small CdSe NCs with respect to that of the large PbSe NCs, even up to a factor of 20. This provides strong evidence that at $\gamma = 0.53$ and high T (70 °C) the $PbSe(CdSe)_2$ AlB_2 structure is the only stable binary superlattice structure coexisting with the single-component crystal structures. This result is in accordance with the theoretical phase diagram of binary hard-sphere mixtures.

In the second size ratio range $0.54 \leq \gamma \leq 0.61$, the theoretical phase diagrams of binary hard-sphere mixtures predict that the binary crystal structures AlB_2 and $NaZn_{13}$ are both stable.[17−19] Note that the latter is only stable at sufficiently high particle number ratio of small to large hard spheres. Solvent evaporation at high temperature (70 °C) from suspensions that combine large PbSe and small CdSe semiconductor NCs with size ratio $\gamma = 0.56$ results in NC films that show four different superlattices: the two fcc lattices, and the binary $PbSe(CdSe)_2$ AlB_2 and $PbSe(CdSe)_{13}$ $NaZn_{13}$ superlattices (Figure 1). Electron tomography has shown that the $PbSe(CdSe)_{13}$ superlattices are genuine icosahedral $NaZn_{13}$ structures.[9] The effect of changing the particle number ratio is shown in Figure 2. At a particle number ratio CdSe NC/PbSe NC below 4, the $PbSe(CdSe)_2$ AlB_2 structure is the most important binary crystal structure, reaching a maximum coverage at a particle number ratio of about 5. Further increase of the concentration of the small CdSe NCs results in an increasing importance of the $PbSe(CdSe)_{13}$ superlattice, reaching a maximum coverage of about 55% on the TEM grid. At a size ratio $\gamma = 0.59$, there are still $PbSe(CdSe)_2$ AlB_2 domains present, but $PbSe(CdSe)_{13}$ $NaZn_{13}$ is the dominant binary NC superlattice for solvent evaporation at 70 and 20 °C. These results show that for mixtures of two semiconductor nanocrystals, AlB_2 and $NaZn_{13}$ are the stable binary crystal structures for size ratios $0.54 \leq \gamma \leq 0.61$, which is in agreement with the theoretical predictions for binary hard-sphere mixtures.[17−19] In contrast, solvent evaporation from binary suspensions that combine semiconductor PbSe NCs with metallic Au NCs results predominantly in single-component fcc lattices. Several binary crystal structures were observed, though with a minute coverage (≤1%). The absence of substantial amounts of AlB_2 and $NaZn_{13}$ structures provides evidence that with metallic NCs entropy is not the only driving force in the formation of superlattices.

In the third range, $0.64 \leq \gamma \leq 0.75$, the theoretical phase diagrams of binary hard-sphere mixtures show no stable binary structures (Supporting Information). Solvent evapora-

© 2010 American Chemical Society

DOI: 10.1021/nl102705p | *Nano Lett.* **2010,** *10,* 4235–4241

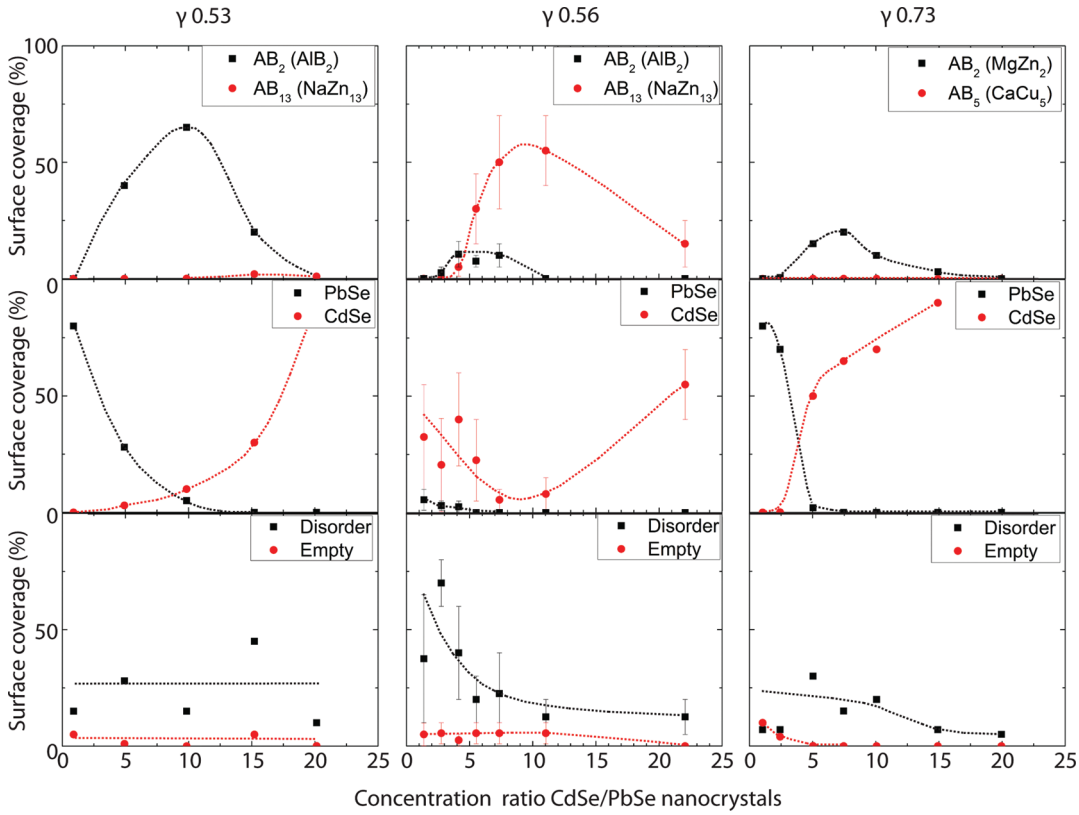

FIGURE 2. The effect of changing the particle concentration ratio in the binary mixtures on the relative importance of the formed single-component and binary NC superlattices. The size ratio of the large PbSe NCs with respect to the small CdSe NCs is $\gamma = 0.53$ (left panels), $\gamma = 0.56$ (center panels), and $\gamma = 0.73$ (right panels). The dotted lines are guides to the eye. The size ratio of 0.56 is from former published work.[11] The uncertainty on the % surface coverage is about 25 relative %.

tion at 70 °C of suspensions that contain large PbSe and smaller CdSe NCs ($\gamma = 0.65$ and 0.72) shows nanocrystal films that contain predominantly single-component lattices. Minute fractions of binary NC superlattices that contain $CaCu_5$ and $MgZn_2$ are also observed. Free-energy calculations show that $CaCu_5$ is not stable for this size ratio range (Supporting Information). At $\gamma = 0.73$, however, the $MgZn_2$ becomes the dominant binary crystal structure, coexisting with the single-component fcc lattice and a minute fraction of $CaCu_5$. If the concentration of the small CdSe NCs is increased with respect to that of the larger PbSe NCs, the $MgZn_2$ phase reaches a maximum surface coverage of 25% at around a particle concentration ratio CdSe NC/PbSe NC of 7. When the relative concentration of the smaller CdSe particles is increased further, the single-component CdSe superlattice becomes dominant. Strikingly, the $PbSe(CdSe)_5$ superlattice ($CaCu_5$) is only marginally present in the entire range of relative particle concentration, showing that this phase is very likely not thermodynamically stable. We conclude that $PbSe(CdSe)_2$ ($MgZn_2$) is a thermodynamically stable phase at $\gamma = 0.73$, hence at a size-ratio slightly smaller than predicted by simulations ($\gamma = 0.76$).[20] The same conclusion holds for a size ratio γ of 0.75. Using this combination of PbSe and CdSe NCs, we have also performed solvent evaporation experiments at temperatures below 70 °C. In Figure 3, typical overviews of the nanocrystal films formed at 70 and 20 °C are presented. At 70 °C, 95% of the binary structures consists of $PbSe(CdSe)_2$ ($MgZn_2$) with a minor fraction (5%) of PbSe(CdSe), isostructural with cubic CsCl. Solvent evaporation at 20 °C, however, leads to a reduction of the $MgZn_2$ fraction (50−1% of the binary crystals, depending on the sample) and an increase of the CsCl structure (50−99% of the binary crystals). These results show that reducing the temperature leads to new structures that are not stable in the theoretical phase diagrams of binary hard-sphere mixtures. Hence, energetic interactions between the nanocrystals become important when the temperature is lowered.

Recent theoretical work has shown the Laves phases ($MgZn_2$, $MgCu_2$, $MgNi_2$,) to be stable in the size ratio range $0.76 \leq \gamma \leq 0.84$.[20] In accordance with this prediction, the combination of PbSe and CdSe NCs at $\gamma = 0.79$ and $\gamma = 0.80$ leads to $PbSe(CdSe)_2$ superlattices with a $MgZn_2$ structure. However, this binary crystal structure constitutes only a small fraction of the NC film that consists mainly of single-component lattices. Apart form the $MgZn_2$ structure, the other Laves phases were not observed. Indeed, a finite-size scaling analysis shows that the free-energy difference between the three Laves structures is small, but that $MgZn_2$ has the lowest free energy in the thermodynamic limit.[20] In

© 2010 American Chemical Society

DOI: 10.1021/nl102705p | *Nano Lett.* **2010,** *10,* 4235–4241

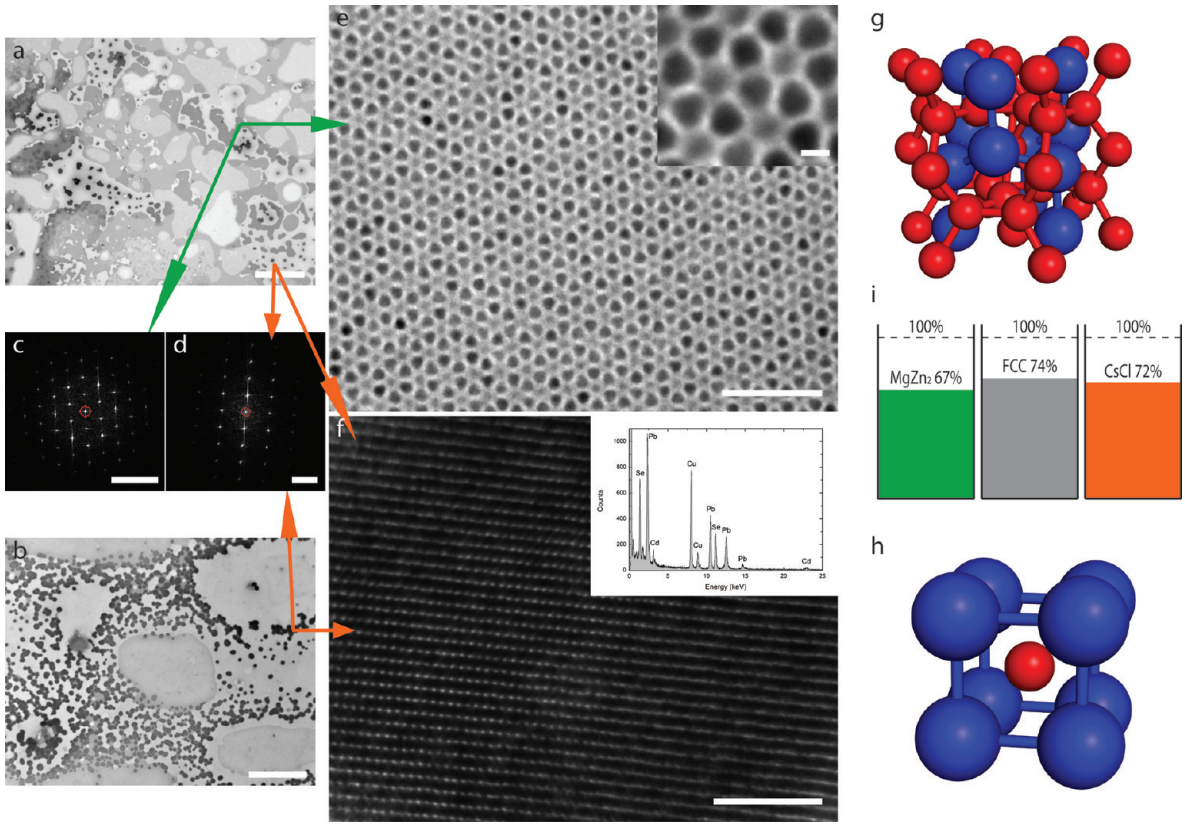

FIGURE 3. Binary superlattices formed from a suspension of large PbSe nanocrystals (7.76 nm effective diameter) and smaller CdSe nanocrystals (5.8 nm effective diameter) by solvent evaporation at 70 and 20 °C; the particle size ratio γ is 0.75, and particle concentration ratio is 2. (a,b) Overview of the structures observed on the TEM grid after solvent evaporation at 70 and 20 °C, respectively. (c,e,g) Fourier transform, TEM projection, and unit cell of the PbSe(CdSe)2 lattice isostructural with MgZn2. (d,f,h) Fourier transform, TEM projection, and unit cell of the PbSe(CdSe) lattice isostructural with CsCl; the insert in f shows the results of EDX elemental analysis providing evidence for a binary structure of PbSe and CdSe nanocrystals. The scale bars for panels a and b are 5 μm, panels c and d are 0.25 nm^{-1}, panels e and f are 50 nm, and 5 nm for the inset of panel e.

accordance with this, using a combination of CdTe and CdSe NCs, Chen et al. observed the $MgZn_2$ phase at $\gamma = 0.81$.[8] We remark that with mixtures of micrometer-sized hard spheres, Laves phases have not been observed yet. The combination of metallic Au NCs with PbSe NCs results in NC films with an important contribution of CsCl (up to 30%) in coexistence with the single-component phase. Free energy simulations show that this structure can only be stabilized if interparticle interactions are incorporated.

Colloidal Crystallization by Addition of a Nonsolvent. Adding a nonsolvent leads to increased van der Waals attractions between the NCs, inducing colloidal crystallization even at low particle concentration. We have studied the crystal structures that were formed in binary mixtures of large PbSe and small CdSe NCs, and large PbSe and small Au NCs in hexane to which butanol was added as a nonsolvent. The experiments were performed in a broad size ratio range $0.53 \leq \gamma \leq 0.98$. Binary crystal structures were never observed. Instead, 3D colloidal crystals consisting exclusively of the larger NCs were formed as confirmed by TEM-EDX analysis (see Supporting Information, Figure S2).

Discussion. A summary of the observed crystal structures compared with the theoretical results for binary hard-sphere mixtures is presented in Figure 4. The binary NC superlattice structures $PbSe(CdSe)_2$ iso-structural with AlB_2, $PbSe(CdSe)_{13}$ iso-structural with $NaZn_{13}$, and $PbSe(CdSe)_2$ iso-structural with $MgZn_2$ obtained from binary mixtures of organically capped semiconductor NCs in a good solvent at sufficiently high temperature are as expected on the basis of binary hard-sphere phase diagrams. Similar results were obtained by Chen et al., who combined CdTe and CdSe NCs.[8,10] Unlike the latter, we have also investigated the effect of changing the particle concentration ratio in the suspension. We find that, for each of the three stable binary structures, the relative importance in the film depends on the composition of the initial suspension. For instance at $\gamma = 0.53$, the importance of the stable $PbSe(CdSe)_2$ structure increases to a maximum at a particle concentration ratio CdSe/PbSe of 10, this happens at the expense of the PbSe fcc structure. At higher CdSe/PbSe ratios, the importance of the binary structure decreases, and the fcc CdSe lattice becomes the dominant structure. Such a correlation between the composition of the suspension and the stoichiometry of the film forms a landmark for true equilibrium structures. Combining two types of semiconductor NCs at high temperature, we

© 2010 American Chemical Society

DOI: 10.1021/nl102705p | *Nano Lett.* **2010,** *10,* 4235–4241

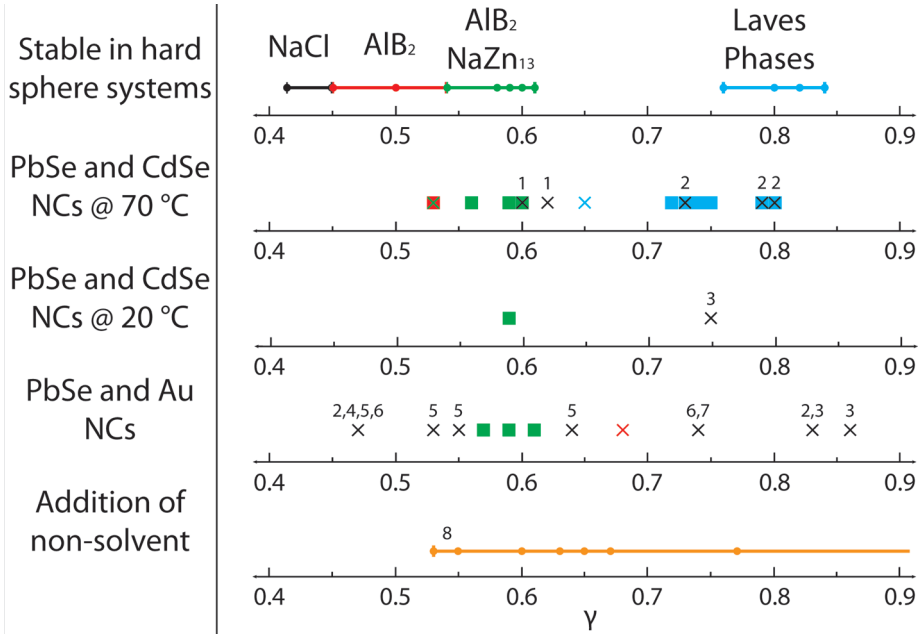

FIGURE 4. Schematic comparison of the structures that are experimentally observed with the theoretical phase diagrams for binary hard-sphere mixtures. Squares indicate crystal structures that are in agreement with the hard-sphere model. Crosses indicate crystal structures that are in disagreement with the hard sphere model: (1) refers to several unknown crystal structures (Supporting Information Figure SI3), coverage <1%; (2) $PbSe(CdSe)_5$ isostructural with $CaCu_5$, coverage <1%, the coverage does not respond to a change in the composition; (3) CsCl structure; (4) NaCl structure; (5) CuAu structure; (6) Cu_3Au structure. The crystal structures (1−6) have a low (∼1%) surface coverage. The number 7 indicates the CsCl crystal structure, observed here with a surface coverage of about 30%. Number 8 is for the addition of a nonsolvent for which only single-component structures are observed.

did not observe any dominant crystal structure that is in flagrant disagreement with the theoretical predictions for binary hard-sphere mixtures. It should be realized that the contribution due to the van der Waals interactions (see Supporting Information, Sections II and III) between the NCs can become important to the free-energy when the conditions for self-organization are slightly changed. For instance, while at 70 °C the combination of PbSe and CdSe NCs leads to the formation of the $MgZn_2$ binary superlattice in agreement with the hard-sphere phase diagrams, lowering of the temperature leads to a gradual increase of the CsCl structure that is not stable for binary hard-sphere mixtures. Second, when one of the particles is metallic, the van der Waals attractions are increased, and several binary crystal structures are observed that can only be stabilized by energetic interactions (see Figure 4, PbSe and Au NCs). In line with this, we also found that a gradual increase of the interactions between the nanocrystals induced by adding a nonsolvent leads solely to single-component crystal structures. We should remark here that the somewhat larger size polydispersity of the Au NC suspension (10%) is not expected to have a strong influence on the type of superlattices that are formed. First, a polydispersity of ∼8% can still be tolerated in an fcc lattice,[22,23] and we expect that this also holds for the hard-sphere binary superlattices since they have a similar filling fraction. If, however, the polydispersity exceeds ∼8%, fractionation into different fcc phases is predicted. We did not observe this. The only apparent effect of the 10% polydispersity was the increased occurrence of disordered regions, possibly composed of the particles that were not fitted in the main fcc and binary superlattices.

Our work shows that under certain conditions, that is, two types of semiconductor NCs in a good solvent at high temperature, the formation of binary nanocrystal superlattices is driven by an increase in entropy. When these conditions are not fulfilled, interactions must be taken into account to understand the resulting superlattices. Our findings are of importance for the design of novel 3D nanostructured materials from the huge variety of nanocolloids now available. It is clear that if colloidal crystallization is driven solely by entropy, the resulting binary superlattice structures are determined only by the size-ratio of the nanocrystals and the relative particle concentrations in the suspension. This simplicity opens avenues to the rational design of two-component nanostructured semiconductors. These systems hold promise for novel types of miniaturized transistors, thermoelectric materials, and photovoltaics.

Methods. PbSe NCs were synthesized by a method described by Houtepen et al.[24] The synthesis was performed in a water and oxygen free environment. (1) A 1.9 g sample of lead acetate trihydrate (99.999% Aldrich), 4 mL of diphenyl ether (99% DPE, aldrich), 3 mL of oleic acid (OA, 90% Aldrich), and 16 mL of trioctyl phospine (TOP, 90% Fluka) were heated to 100 °C under low pressure (10−3 bar) for ∼3 h. (2) A second mixture containg 0.31 g of Se (99.999% Alfa Aesar) and 4 mL of TOP was prepared. Subsequently 11.5 mL of solution (1) and 1.7 mL of solution (2) was injected into 10 mL 190 °C DPE. The reaction

© 2010 American Chemical Society

DOI: 10.1021/nl102705p | *Nano Lett.* **2010,** *10,* 4235–4241

mixture was kept at a constant temperature of 145 °C. After 30 s to 10 min the reaction mixture was quenched with 20 mL butanol and 10 mL methanol. The crude synthesis mixtures were washed twice by precipitating with methanol, centrifugation, and redispersion of the sediment in toluene.

CdSe NCs were synthesized by a method described by de Mello Donega et al.[25] The synthesis was performed in a water- and oxygen-free environment. A 0.79 g sample of selenium (99.999% Alfa Aesar), 0.28 g of dimethylcadmium (99.99% ARC Technologies), and 10 mL of TOP (96% Aldrich) was prepared. The solution was injected into a mixture of 20 g of dried trioctylphospineoxide (TOPO, 99% Aldrich) and 10 g of hexadecylamine (HDA) at a temperature of ~300 °C, resulting in a temperature drop to ~170 °C. The temperature was raised and stabilized to the desired growth temperature of 240 °C for 30 min, resulting in nanocrystals with a diameter of approximately 3 nm. The synthesis mixtures were washed twice by precipitating with methanol, centrifugation, and redispersion of the sediment in toluene.

Au NCs were synthesized by a method described by Brust et al.[26] The synthesis was performed at room temperature in ambient environment. (1) A 0.27 g sample of $HAuCl_4$ (99.9%, Aldrich) was desolved in 22.29 g of ultrapure water. (2) A second mixture of 1.90 g of tetraoctylammonium bromide (TOAB, 98%, Aldrich) dissolved in 60 g of toluene (99.8%, Aldrich). 5.3 mL of (1), and 14.8 g of (2) were mixed and stirred vigorously. A third stock solution (3) was prepared by adding 0.076 g of sodium borohydride (98%, Aldrich) to 4.86 g of ultrapure water. Subsequently (3) was rapidly injected in the mixture of (1) and (2). The solution was stirred for ~18 h and afterward 75 μL of 1-dodecanethiol (≥97%, Fluka) was added to the mixture. The sample was washed twice by precipitating with ethanol, centrifugation, and redispersion of the sediment in toluene.

Superlattice formation was achieved by mixing two colloidal suspensions, either PbSe or CdSe or PbSe and Au NC suspensions. The concentration ratio and temperature were varied. Colloidal crystallization was achieved on a TEM grid that makes an angle of 30° with the suspension surface, evaporating the solvent at a temperature of 70 °C under reduced pressure (~10 mbar).

Acknowledgment. W.H.E. and D.V. wish to acknowledge NWO-CW for financial support (Topgrant 700.53.308). D.V. wishes to acknowledge the ITN "HERODOT" (214954) for financial support. L.F. and M.D. wish to acknowledge financial support from the High Potential Program from Utrecht University and the NWO Vici Grant.

Supporting Information Available. Overviews of the obtained crystal structures and relative importance for the combinations PbSe with CdSe NCs and PbSe with Au NCs. Additional TEM and SEM images of the obtained superlattices including novel superlattice structures. Elaboration of the used hard-sphere theory and a theoretical study of the parameters influencing the binary self-assembly. This material is available free of charge via the Internet at http://pubs.acs.org.

REFERENCES AND NOTES

(1) Murray, C. B.; Kagan, C. R.; Bawendi, M. G. *Science* **1995**, *270* (5240), 1335–1338.
(2) Rogach, A. L.; Talapin, D. V.; Shevchenko, E. V.; Kornowski, A.; Haase, M.; Weller, H. *Adv. Funct. Mater.* **2002**, *12* (10), 653–664.
(3) Urban, J. J.; Talapin, D. V.; Shevchenko, E. V.; Kagan, C. R.; Murray, C. B. *Nat. Mater.* **2007**, *6* (2), 115–121.
(4) Heath, J. R. *Nature* **2007**, *445* (7127), 492–493.
(5) Kiely, C. J.; Fink, J.; Brust, M.; Bethell, D.; Schiffrin, D. J. *Nature* **1998**, *396* (6710), 444–446.
(6) Shevchenko, E. V.; Talapin, D. V.; Kotov, N. A.; O'Brien, S.; Murray, C. B. *Nature* **2006**, *439* (7072), 55–59.
(7) Redl, F. X.; Cho, K. S.; Murray, C. B.; O'Brien, S. *Nature* **2003**, *423* (6943), 968–971.
(8) Chen, Z.; Moore, J.; Radtke, G.; Sirringhaus, H.; O'Brien, S. *J. Am. Chem. Soc.* **2007**, *129* (50), 15702–15709.
(9) Friedrich, H.; Gommes, C. J.; Overgaag, K.; Meeldijk, J. D.; Evers, W. H.; Nijs, B. d.; Boneschanscher, M. P.; de Jongh, P. E.; Verkleij, A. J.; de Jong, K. P.; van Blaaderen, A.; Vanmaekelbergh, D. *Nano Lett.* **2009**, *9* (7), 2719–2724.
(10) Chen, Z.; O'Brien, S. *ACS Nano* **2008**, *2* (6), 1219–1229.
(11) Overgaag, K.; Evers, W.; de Nijs, B.; Koole, R.; Meeldijk, J.; Vanmaekelbergh, D. *J. Am. Chem. Soc.* **2008**, *130* (25), 7833–7835.
(12) Shevchenko, E. V.; Talapin, D. V.; O'Brien, S.; Murray, C. B. *J. Am. Chem. Soc.* **2005**, *127* (24), 8741–8747.
(13) Rogach, A. L. *Angew. Chem., Int. Ed.* **2004**, *43* (2), 148–149.
(14) Majumdar, A. *Science* **2004**, *303* (5659), 777–778.
(15) Wang, R. Y.; Feser, J. P.; Lee, J.-S.; Talapin, D. V.; Segalman, R.; Majumdar, A. *Nano Lett.* **2008**, *8* (8), 2283–2288.
(16) Bartlett, P.; Ottewill, R. H.; Pusey, P. N. *Phys. Rev. Lett.* **1992**, *68* (25), 3801.
(17) Trizac, E.; Eldrigde, M. D.; Madden, P. A. *Mol. Phys.* **1997**, *90* (4), 675–678.
(18) Eldridge, M. D.; Madden, P. A.; Pusey, P. N.; Bartlett, P. *Mol. Phys.* **1995**, *84* (2), 395–420.
(19) Eldridge, M. D.; Madden, P. A.; Frenkel, D. *Nature* **1993**, *365* (6441), 35–37.
(20) Hynninen, A. P.; Filion, L.; Dijkstra, M. *J. Chem. Phys.* **2009**, *131* (6), No. 064902−9.
(21) Eldrige, M. D.; Madden, P. A.; Frenkel, D. *Mol. Phys.* **1993**, *79* (1), 105).
(22) Sollich, P.; Wilding, N. B. *Phys. Rev. Lett.* **2010**, *104* (11), 118302.
(23) Sear, R. P. *Europhys. Lett.* **1998**, *44* (4), 531.
(24) Houtepen, A. J.; Koole, R.; Vanmaekelbergh, D.; Meeldijk, J.; Hickey, S. G. *J. Am. Chem. Soc.* **2006**, *128* (21), 6792–6793.
(25) de Mello Donega, C.; Hickey, S. G.; Wuister, S. F.; Vanmaekelbergh, D.; Meijerink, A. *J. Phys. Chem. B* **2003**, *107* (2), 489–496.
(26) Brust, M.; Walker, M.; Bethell, D.; Schiffrin, D. J.; Whyman, R. *J. Chem. Soc, Chem. Commun.* **1994**, 801–802.

© 2010 American Chemical Society

DOI: 10.1021/nl102705p | *Nano Lett.* **2010,** *10,* 4235–4241

Supplementary Information

W.H. Evers,* B. de Nijs,* L. Filion,† S. Castillo,* M. Dijkstra,† and D. Vanmaekelbergh*
Debye Institute for Nanomaterials Science, Utrecht University, The Netherlands

I. ADDITIONAL EXPERIMENTAL PLOTS

size ratio (effective)	Diameter NC (nm)		BNSLs obtained	2D surface coverage (%)
	Large	*Small*		
0.53	11.0 (PbSe)	5.8 (CdSe)	AlB_2	60
			$NaZn_{13}$	1
			Single component	10
0.56	10.3 (PbSe)	5.8 (CdSe)	AlB_2	10
			$NaZn_{13}$	60
			Single component	10-20
0.59 (2) T=70 °C	9.8 (PbSe)	5.8 (CdSe)	AlB_2	<1
			$NaZn_{13}$	5-15
			Single component	40-60
0.59 (2) T=20 °C	9.8 (PbSe)	5.8 (CdSe)	AlB_2	<1
			$NaZn_{13}$	10-20
			Single component	5-15
0.6	9.61 (PbSe)	5.8 (CdSe)	AlB_2	<1
			$NaZn_{13}$	<1
			unknown	<1
			Single component	10-80
0.62	9.43 (PbSe)	5.8 (CdSe)	AlB_2	<1
			$NaZn_{13}$	<1
			unknown	<1
			Single component	20-60
0.65	8.88 (PbSe)	5.8 (CdSe)	$MgZn_2$	<1
			$CaCu_5$	<1
			Single component	
0.72	8.09 (PbSe)	5.8 (CdSe)	$MgZn_2$	<1
			Single component	>50
0.73	8.0 (PbSe)	5.8 (CdSe)	$MgZn_2$	25
			$CaCu_5$	1
			Single component	40-60
0.75 T=70°C	7.76 (PbSe)	5.8 (CdSe)	$MgZn_2$	10-15
			CsCl	<1-5
			Single component	20-50
0.75 T=20°C	7.76 (PbSe)	5.8 (CdSe)	$MgZn_2$	<1-7
			CsCl	10-15
			Single component	20-40
0.79	7.37 (PbSe)	5.8 (CdSe)	$MgZn_2$	<1
			$CaCu_5$	<1
			Single component	20-80
0.8	7.23 (PbSe)	5.8 (CdSe)	$MgZn_2$	<1
			$CaCu_5$	<1
			Single component	30-80

TABLE 1: Overview of the superlattices obtained by solvent evaporation from binary suspensions of semiconductor nanocrystals, i.e. combinations of PbSe NC and CdSe NC with varying size ratio $\gamma = \sigma_S/\sigma_L$, where $\sigma_{S(L)}$ is the diameter of the small (large) particles. Solvent evaporation was performed at 70°C (unless otherwise stated). The relative importance of the different structures that are formed are expressed in maximum % surface coverage.

*Condensed Matter and Interfaces
†Soft Condensed Matter

size ratio (effective)	Diameter NC (nm)		Crystal structure	2D surface coverage (%)
	Large	*Small*		
0.47	11.0 (PbSe)	5.2 (Au)	NaCl	1-5
			CuAu	<1
			Cu_3Au	<1
			$CaCu_5$	<1
			Single component	10-50
0.53	9.8 (PbSe)	5.2 (Au)	CuAu	<1
			Single component	10-20
0.55	9.49 (PbSe)	5.2 (Au)	CuAu	<1
			Single component	10-20
0.57	9.8 (PbSe)	5.58 (Au)	$NaZn_{13}$	<1
			Single component	1-20
0.59	11.0 (PbSe)	6.59 (Au)	AlB_2	<1
			Single component	10-50
0.61	9.49 (PbSe)	5.8 (Au)	AlB_2	<1
			Single component	10-50
0.64	9.8 (PbSe)	6.29 (Au)	CuAu	1-5
			Single component	30-50
0.68	11.0 (PbSe)	7.51 (Au)	AlB_2	<1
			Single component	10-50
0.74	6.98 (PbSe)	5.2 (Au)	CsCl	20-30
			Single component	10-30
0.83	6.98 (PbSe)	5.8 (Au)	CsCl	1-10
			$CaCu_5$	1-5
			Single component	10-50
0.86	8.1 (Au)	6.98 (PbSe)	CsCl	<1
			Single component	30-50

TABLE 2: Overview of the superlattices formed from a PbSe NC / Au NC suspension for different size ratios γ. The relative importance of the structures that are formed are expressed as maximum % coverage of the total surface area examined. The solvent evaporation was performed at 70°C.

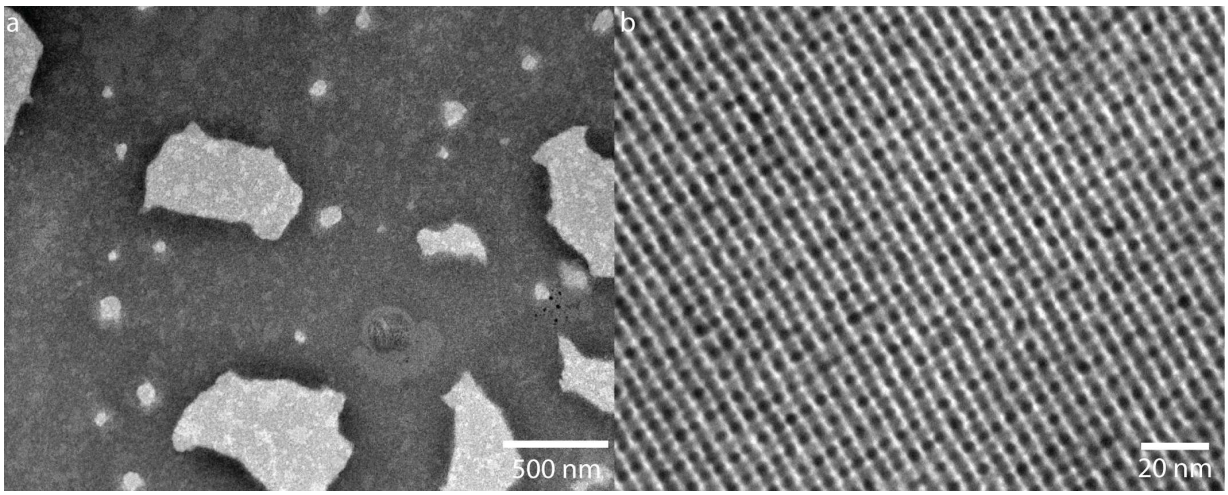

FIG. S1: Binary and single-component superlattices obtained from a suspension of PbSe nanocrystals (7.0 nm effective diameter) and Au nanocrystals (5.2 nm effective diameter) at a size ratio $\gamma = 0.74$. (a) overview of the TEM grid with single component domains of PbSe and Au NCs, binary domains PbSe(Au), iso-structural with CsCl. (b) detailed TEM image showing a binary PbSe(Au) superlattice with CsCl structure.

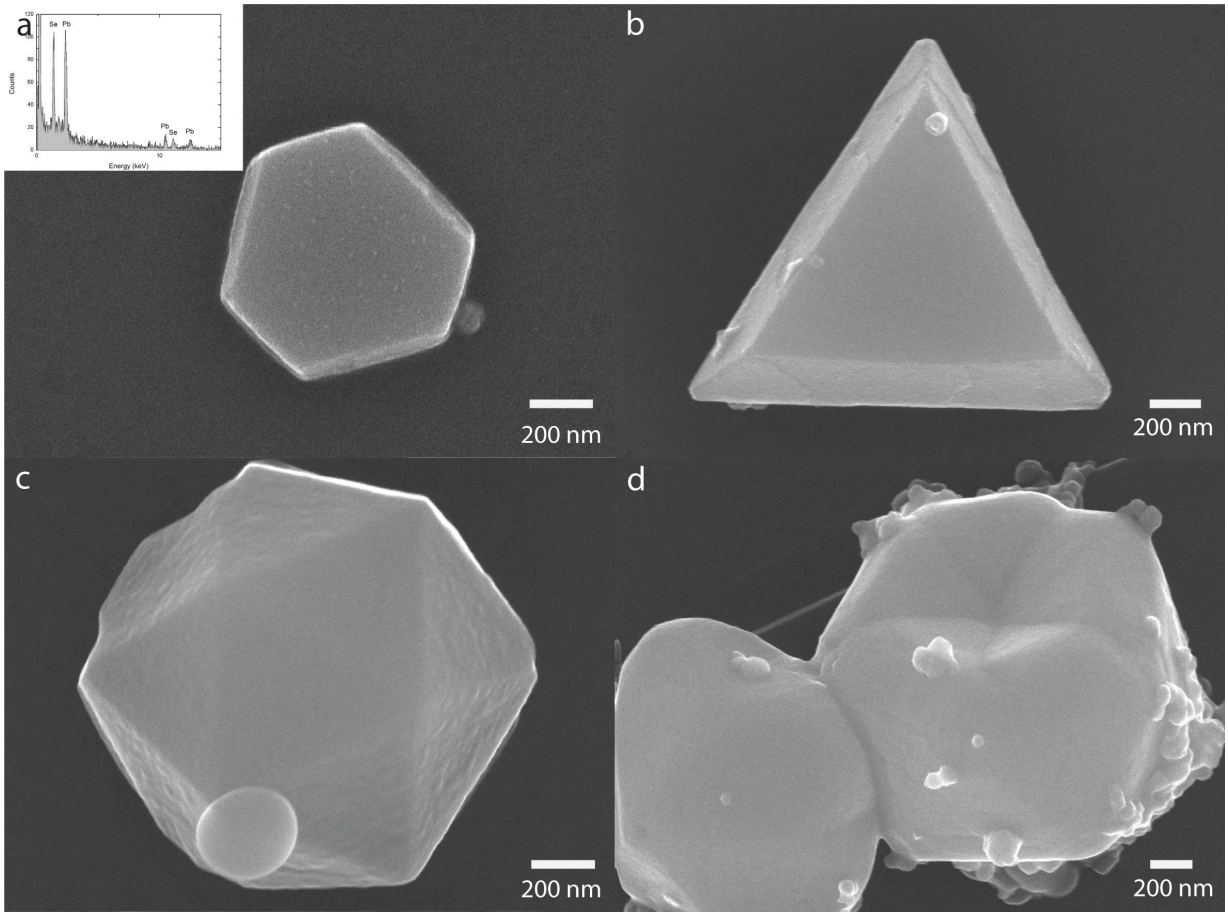

FIG. S2: Crystals obtained due to addition of a non-solvent to a binary suspension consisting of large PbSe NCs and smaller CdSe or Au NCs. The size ratio γ was varied between 0.53 and 0.98. Only single-component superlattices consisting of the larger PbSe NC were observed. Different crystal shapes are found: (a) hexagonal platelet, (b) triangular platelet, (c) icosahedron, (d) collapsed icosahedrons. In the inset of (a), an EDX spectrum is given, indicating the presence of PbSe NCs only.

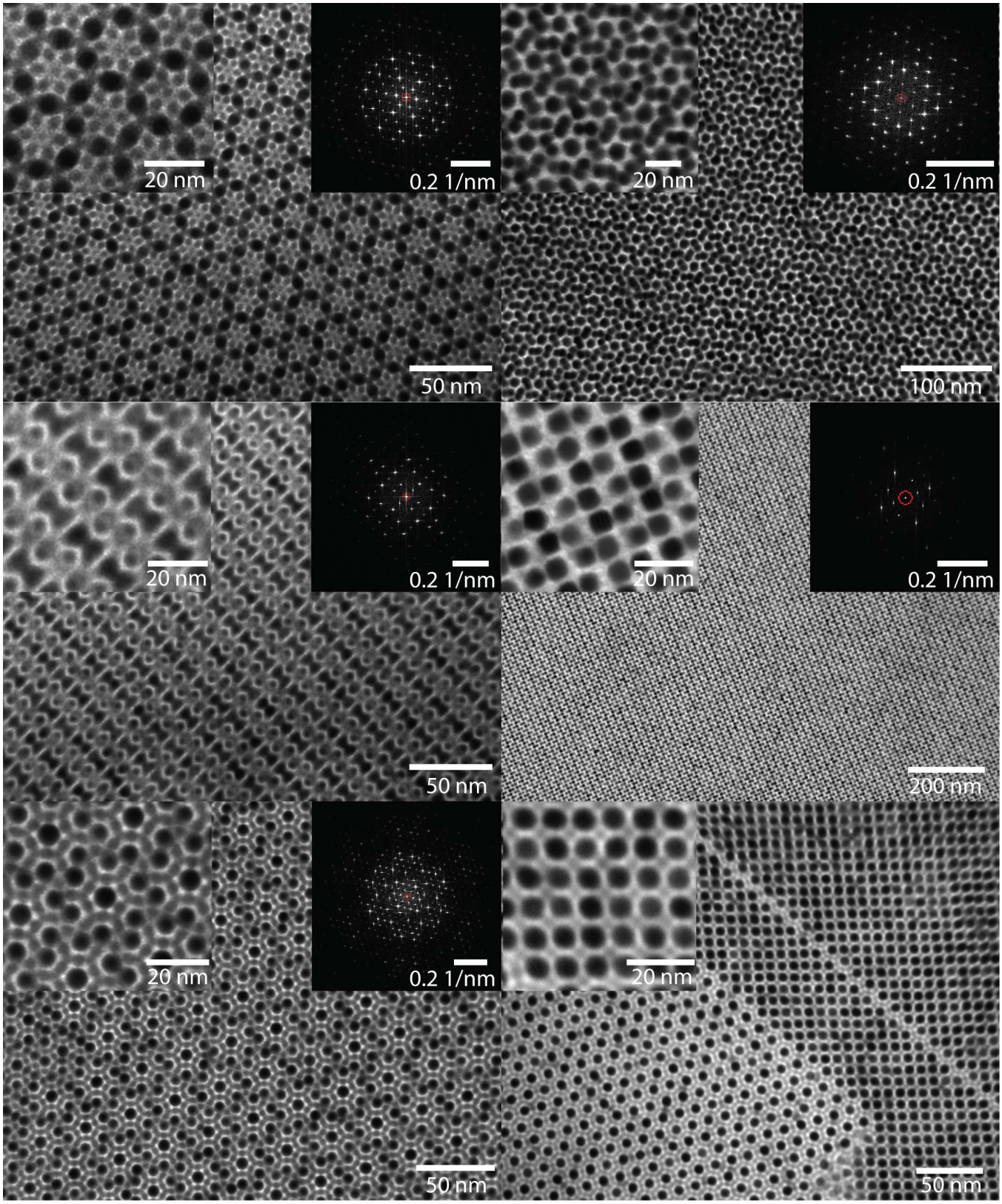

FIG. S3: Unknown binary superlattices obtained from PbSe and CdSe NCs at a size ratio γ between 0.60-0.63. In the inset of each of the images, a zoom in of the TEM pictures of the crystal structure and a Fourier transform are presented.

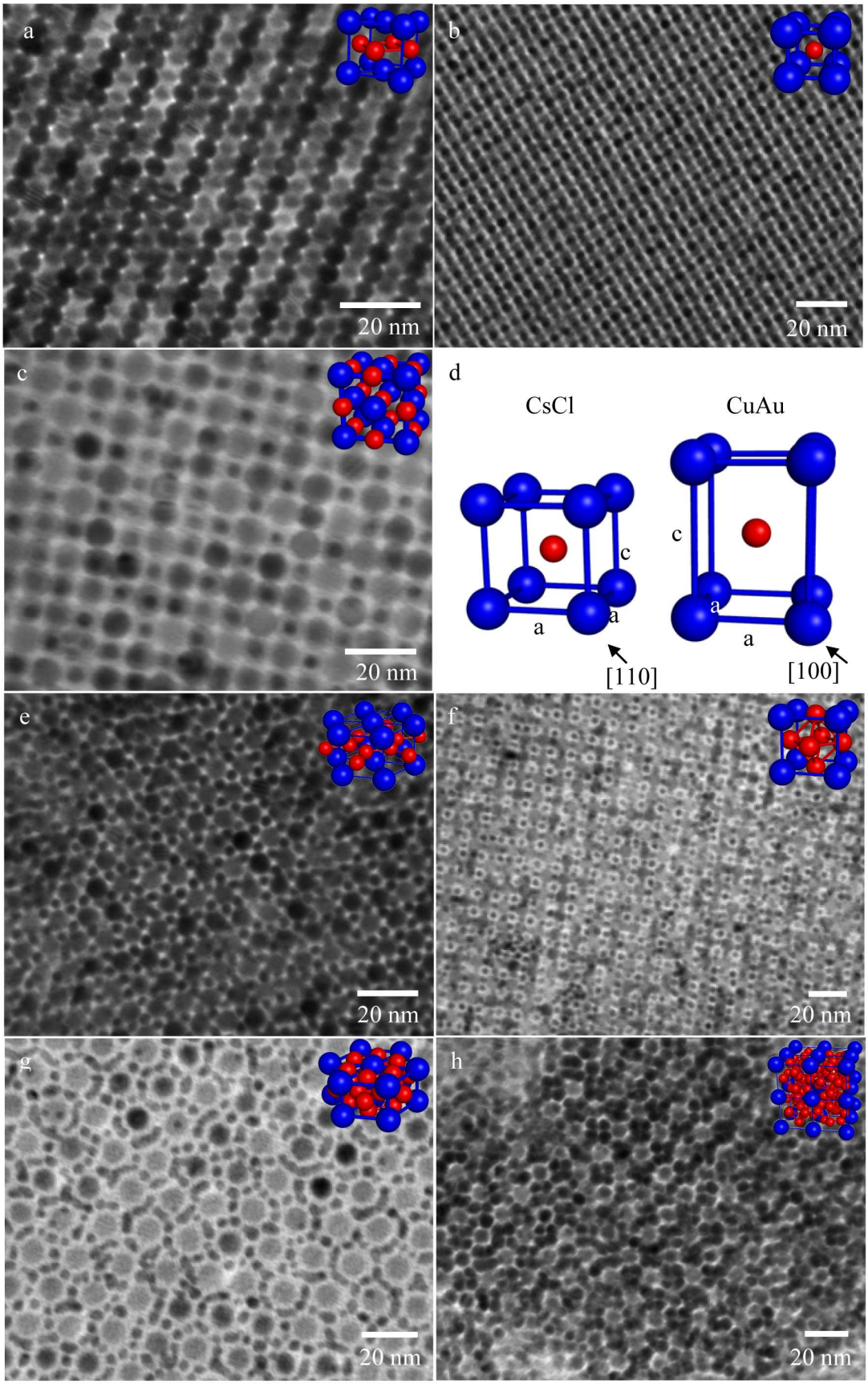

FIG. S4: Binary superlattices obtained by colloidal crystallization at 70°C from suspensions of PbSe and Au nanocrystals. (a)-(c) Binary superlattices with AB stoichiometry (a) CuAu structure ($\gamma = 0.53$), (b) CsCl structure ($\gamma = 0.74$), (c) NaCl structure ($\gamma = 0.47$). (d) Cartoon showing the difference between CsCl and CuAu structure. The CsCl structure consists of a cubic lattice of the large particles where the axes of the unit cell are all equal, while the CuAu structure has one prolonged axis. (e) AlB_2 structure ($\gamma = 0.61$). (f) Cu_3Au ($\gamma = 0.47$). (g) $CaCu_5$ structure ($\gamma = 0.83$). (h) $NaZn_{13}$ structure ($\gamma = 0.57$).

II. BINARY HARD SPHERE MIXTURES

A. Summary of Theoretical Results

In Table 3 we list all the binary crystal structures which are predicted to be stable in the phase diagrams of binary hard-sphere mixtures obtained from full free-energy calculations for various size ratios $\gamma = \sigma_S/\sigma_L$ where $\sigma_{S,L}$ is the diameter of the small and large hard spheres, respectively [1–6].

Size Ratio (γ)	Stable Crystal Structures	Reference
0.033	fcc with disordered small	1
0.05	fcc with disordered small	1
0.1	fcc with disordered small	1
0.2	fcc with disordered small	1
0.414	NaCl	2
0.45	NaCl and AlB_2	2
0.50	AlB_2	3
0.54	AlB_2 and ico-AB_{13}	3
0.58	AlB_2 and ico-AB_{13}	3, 4
0.59	AlB_2 and ico-AB_{13}	3
0.60	AlB_2 and ico-AB_{13}	3
0.61	AlB_2 and ico-AB_{13}	3
0.625	ico-AB_{13}	3
0.74	only fcc_L and fcc_S	5
0.76	Laves Phases ($MgZn_2$, $MgCu_2$, $MgNi_2$)	5
0.80	Laves Phases ($MgZn_2$, $MgCu_2$, $MgNi_2$)	5
0.82	Laves Phases ($MgZn_2$, $MgCu_2$, $MgNi_2$)	5
0.84	Laves Phases ($MgZn_2$, $MgCu_2$, $MgNi_2$)	5
0.85	eutectic solidsolution	6
0.875	eutectic solidsolution	6
0.90	azeotropic	6
0.92	azeotropic	6
0.9425	azeotropic	6
0.95	fcc solid solution (spindle)	6

TABLE 3: A list of all the structures which have been shown to be stable in hard-sphere systems as a function of the size ratio γ.

B. Binary Hard-Sphere Mixtures Theory

From thermodynamics, the Helmholtz free energy F of a system consisting of N particles in a volume V, and at temperature T is given by

$$F = U - TS \tag{1}$$

where U is the potential energy, and S is the entropy. For a system consisting of hard spheres the pair potential is given by

$$V_{\rm HS}(r_{ij}, \sigma_i, \sigma_j) = \begin{cases} 0 & r_{ij} > (\sigma_i + \sigma_j)/2 \\ \infty & r_{ij} \leq (\sigma_i + \sigma_j)/2 \end{cases} \tag{2}$$

where r_{ij} is the distance between particles i and j, and σ_i is the diameter of particle i. Since the Boltzmann weight is zero for configurations that contain particle overlaps, the free energy is determined solely by the entropy. (The potential energy contribution to the free energy for all configurations without overlaps is simply zero, hence only the entropic term is left.)

One method of calculating the exact free energy for a general system, such as hard-sphere mixtures, is thermodynamic integration. In this case, it is assumed that there exists a reference system for which we can calculate the free energy analytically. For example, for liquids often the ideal gas is used and for crystals, the Einstein crystal can serve as the reference system. If the potential energy of the reference system is given by U_R and the potential energy of

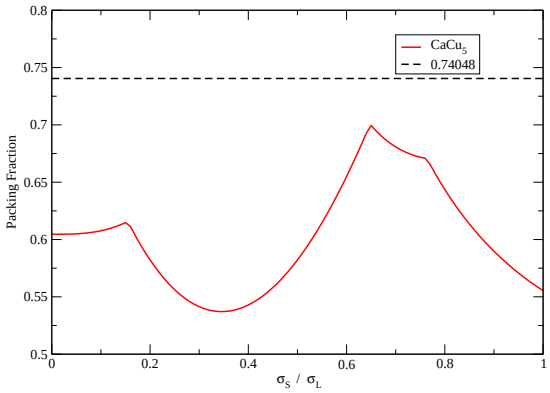

FIG. S5: Maximum packing fraction of $CaCu_5$ as a function of the size ratio σ_S/σ_L.

our true system of interest is denoted U_T then it is possible to define a new (fictitious) potential energy

$$U(\lambda) = (1-\lambda)U_T + \lambda U_R, \tag{3}$$

which is now a function of a coupling parameter λ, which varies between 0 and 1. Note that this function has the property that when $\lambda = 0$ it reduces to our system of interest, and when $\lambda = 1$ it reduces to the reference system. The free-energy difference between the reference and the system of interest can be determined exactly, see Ref. 7, and is given by

$$F(\lambda=1) - F(\lambda=0) = \int_{\lambda=0}^{\lambda=1} d\lambda \left\langle \frac{\partial U(\lambda)}{\partial \lambda} \right\rangle_\lambda . \tag{4}$$

Thus, to calculate the free energy exactly we simply need to determine $\langle \partial U(\lambda)/\partial\lambda \rangle_\lambda$ as a function of λ. Such an average can be determined using a Monte Carlo simulation. Additionally, after the Helmholtz free energy is known, all other relevant thermodynamic quantities (such as the Gibbs free energy) can then be obtained.

Once the free energies are known, techniques such as common tangent constructions are used to determine the phase diagrams, and thus, the stability of various candidate phases. Such methods make use of the fact that the temperature, pressure and chemical potential of all the species must be equal in the coexisting phases when the system is in thermodynamic equilibrium. Equivalently, the system always chooses the state with the lowest total Gibbs free energy. Specifically, the system will choose a linear combination of phases such that the total Gibbs free energy is minimized.

C. Stability of $CaCu_5$

To study the stability of the $CaCu_5$ structure as a candidate crystal structure for a binary hard-sphere system we first examined the maximum packing fraction of the structure as a function of the size ratio γ of the particles. A plot of the maximum packing fraction is shown in Fig. S5.

From Fig. S5 we notice that $CaCu_5$ is most likely to be stable for a size ratio range $0.64 - 0.70$ as the highest possible packing fraction lies within this range. In order to determine whether or not $CaCu_5$ is stable, we calculate the Gibbs free-energy of $CaCu_5$ and compare it with that of phase separated single-component fcc crystals. To calculate the Gibbs free energy of $CaCu_5$ we used the Frenkel-Ladd Einstein integration method as described in Ref. 8 and in Sec. IIB. For the single-component fcc crystals we used the free energy expressions from Ref. 9. For size ratios 0.64, and 0.70, we find that the phase separated fcc phase has a lower Gibbs free energy than that of the $CaCu_5$ structure, indicating that $CaCu_5$ is not thermodynamically stable for binary hard-sphere mixtures.

III. INTERACTIONS

In order to make predictions for the phase behaviour of complex fluids, one often resorts to simplified models in which the degrees of freedom of the microscopic species (solvent, polymer) are formally integrated out so that the macroscopic constituents interact via effective interactions. This is a well-trodden pathway in statistical physics

and has been applied successfully in colloidal science [1, 10–12]. By integrating out the degrees of freedom of the microscopic species in the partition function, one can derive a formal expression for the effective Hamiltonian for the macroscopic species, which include many-body interactions. If the effective pair interactions are sufficiently short-ranged, three- and higher body effective interactions can be neglected and pairwise additivity of the effective pair interactions can be assumed. In the case examined in this paper, particularly in the case of semiconductor nanoparticle mixtures, both the steric interaction and the screened Van der Waals interactions, are short ranged. As a result, pairwise interaction potentials are expected to be a good first approximation for the effective interaction between nanoparticles. In this section, we consider a pairwise potential consisting of a contribution from a Van der Waals (VdWs) interaction between the cores, a steric interaction between the capping ligands, and a hard-sphere replusion between the cores. The effective potential is given by

$$\beta V_{\rm eff}(r_{ij},\sigma_i,\sigma_j) = \beta V_{\rm vdw}(r_{ij},\sigma_i,\sigma_j) + \beta V_{\rm steric}(r_{ij},\sigma_i,\sigma_j) + \beta V_{\rm HS}(r_{ij},\sigma_i,\sigma_j), \tag{5}$$

where r_{ij} is the distance between the center of mass of two nanoparticles i and j, σ_i is the diameter of particle i, $V_{\rm HS}(r_{ij},\sigma_i,\sigma_j)$ is given by Eq. 2, $\beta = 1/k_BT$, k_B is Boltzmann's constant and T is the temperature. We assume that the Van der Waals interaction between the capping layers can be neglected for a monolayer protected nanocrystal in a good solvent.

A. Van der Waals

The Van der Waals interaction between two core-shell particles labelled i and j at distance r_{ij} with diameters $\sigma_{i(j)}$ and Hamaker constant A is given by [13, 14]

$$\beta V_{\rm vdw}(r_{ij},\sigma_i,\sigma_j) = -\frac{\beta A}{12}\left[\frac{S_{ij}}{D_{ij}\left(1+\frac{D_{ij}}{(\sigma_i+\sigma_j)}\right)} + \frac{1}{1+\frac{D_{ij}}{S_{ij}}+\frac{D_{ij}^2}{\sigma_i\sigma_j}} + 2\ln\left(\frac{D_{ij}\left(1+\frac{D_{ij}}{(\sigma_i+\sigma_j)}\right)}{S_{ij}\left(1+\frac{D_{ij}}{S_{ij}}+\frac{D_{ij}^2}{\sigma_i\sigma_j}\right)}\right)\right], \tag{6}$$

where $S_{ij} = \sigma_i\sigma_j/(\sigma_i+\sigma_j)$ and $D_{ij} = r_{ij} - (\sigma_i+\sigma_j)/2$.

For the Hamaker constant, we consider gold-gold interactions, gold-semiconductor interactions, and semiconductor-semiconductor interactions. For the gold-gold interaction we let A=3 eV. We note that values for the gold-gold interaction are found between approximately 1.1 and 3 eV [15–18], where we note that some of the literature has used the fact that the gold-gold Hamaker constant is approximately equal to the silver-silver Hamaker constant. The CdSe-CdSe Hamaker constant across a hydrocarbon layer is approximately 0.3 eV [19]. We assume that this value is general for semiconductors. The semiconductor-gold interaction can be derived (approximately) from these interactions using the relation[15] $A_{12} \approx \sqrt{A_1 A_2}$. Note that we assume no temperature dependence of the Hamaker constant. For a more complete discussion of the Hamaker constant, see Ref. 15.

B. Steric Interactions

To model the steric interaction, we use the Alexander-de Gennes model [15]. This model approximates the interaction between plates with an absorbed polymer layer in a good solvent with a high coverage of the polymer capping molecules. To transform this interaction between plates to an interaction between spheres of diameter σ_i and σ_j we use the Derjaguin approximation [15]. The resulting interaction between the spheres is given by

$$\beta V_{\rm steric}(r_{ij},\sigma_i,\sigma_j) = \begin{cases} \frac{32\pi S_{ij}L^2}{70s^3}\left[28(x_{ij}^{-1/4}-1)+\frac{20}{11}(1-x_{ij}^{11/4})+12(x_{ij}-1)\right] & r_{\rm c} < r_{ij} < r_{\rm c}+2L \\ 0 & \text{otherwise} \end{cases}$$

where $x_{ij} = D_{ij}/(2L)$, $r_c = (\sigma_1+\sigma_2)/2$, s is the mean distance between attachment points of the capping ligands (which we refer to as the ligand distance for the remainder of this paper) and L is the thickness of the capping layer. Here we have made the further approximation that the interaction length and ligand distance of the capping layer are the same for all nanoparticle mixtures. In reality, the ligand distance and thickness of the capping layer can be different between the various semiconductor and gold nanoparticles.

C. Study of Parameters

In this section we study the effect of particle radius, capping ligand distance and capping layer thickness on the effective semiconductor-semiconductor (SC-SC), gold-gold (Au-Au), and semiconductor-gold (SC-Au) interactions.

The various nanoparticles examined in this paper are capped with either dodecanethiol, or a combination of dodecathiol and oleic acid. The interaction length of dodecanethiol on a silver nanoparticle is $L \approx 1.5$ nm [20]. Oleid acid should have a slightly shorter interaction range. For the capping ligand distance, Ref. 20 measures a mean distance of $s \approx 0.43$ nm between the dodecanethiol ligands on a silver nanoparticle. Using these parameters we plot the effective SC-SC, Au-Au, and SC-Au interactions as a function of size ratio (Figs. S6, S7, and S8). We observe that since the VdWs interactions between the nanoparticles are weaker for smaller particles, the steric screening is generally more effective for the smaller particles. Similarly, the weaker VdWs interactions for SC-SC mixtures also result in more effective steric screening as compared to the SC-Au and particularly, Au-Au mixtures. In all cases, the effective interaction displays a strong short-range repulsion and longer-ranged, weak attraction of less than 3 k_BT.

In Figs. S9, S10 and S11, the effect of temperature on the various interaction types is examined. In all cases, the steric interaction screens the VdWs interactions better at higher temperatures. However, the temperature dependence of the screening is almost negligible in the SC-SC interactions which are well screened even at low temperature: the difference between the attraction over the full range of temperatures studied (150-390 K) is much less than 1 k_BT. In contrast, over the same temperature range, the attractive well of the Au-Au effective interactions ranges between approximately 2 to 6 k_BT indicating a much stronger role of temperature in the Au-Au interactions.

The effect of the capping layer thickness is examined in Figs. S12, S13, and S14. In general, the screening of the VdWs interactions is improved by increasing the capping layer thickness, however, the effect is much less important in the case of SC-SC interactions. While the variation of the attractive well for the SC-SC interactions is less than 0.5 k_BT in all cases, in the case of Au-Au effective interactions the well depth can be tuned from approximately 1 to 8 k_BT by varying the capping layer thickness between 2 and 1 nm. Additionally, the effective particle size is strongly effected by the thickness of the capping layer.

Finally, in Figs. S15, S16, and S17 the effect of ligand distance s is examined. Specifically, the effective interactions for SC-SC, Au-Au, and SC-Au nanoparticles is plotted for mean distances between ligand molecules between $s = 0.3 - 0.5$ nm. In general, the distance between the ligand molecules effects the softness of the short-range repulsion, but has no other significant effect in all cases.

In summary, the SC-SC effective interactions have little dependence on the capping layer details, with only slight variations in the softness of the short-range repulsion and attractive well depths never exceeding 1 k_BT over the complete range of parameters examined. Thus, in all cases it appears that the SC-SC interactions are well modelled by a hard-core repulsion, where the only relevant parameters are the relative size ratio between the radius of the particles and the composition of the mixture. The effective length of the capping ligands will effect the relative size ratio between the particles.

In contrast, the temperature, capping layer thickness, and particle size are found to largely effect the Au-Au effective interactions, and to a much smaller extent, the SC-Au interaction. Thus, in modelling SC-Au, or Au-Au mixtures, the details of the ligand coating is expected to be important in determining effective interactions, and, as a result, the resulting phase behaviour of the system.

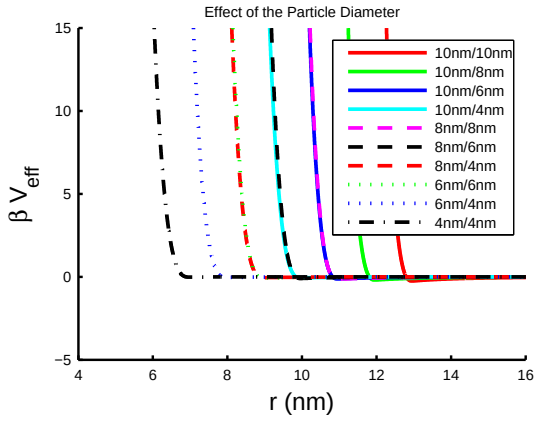

FIG. S6: Effective interactions between two semiconductor nanoparticles for particle diameters as labelled with Hamaker constant $A = 0.3$ eV, capping layer thickness $L = 1.5$ nm, and ligand distance $s = 0.43$ nm at temperature $T = 300$ K.

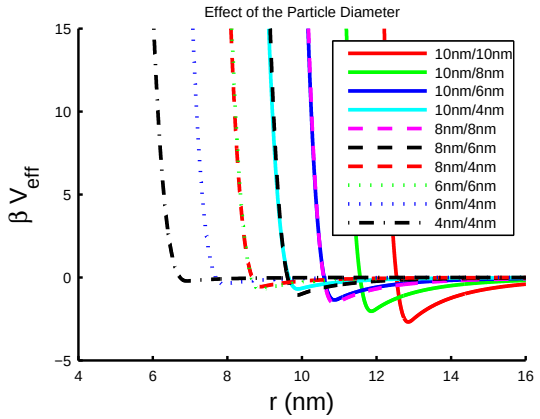

FIG. S7: Effective interactions between two gold nanoparticles for particle diameters as labelled with Hamaker constant $A = 3$ eV, capping layer thickness $L = 1.5$ nm, and ligand distance $s = 0.43$ nm at room temperature ($T = 300$ K).

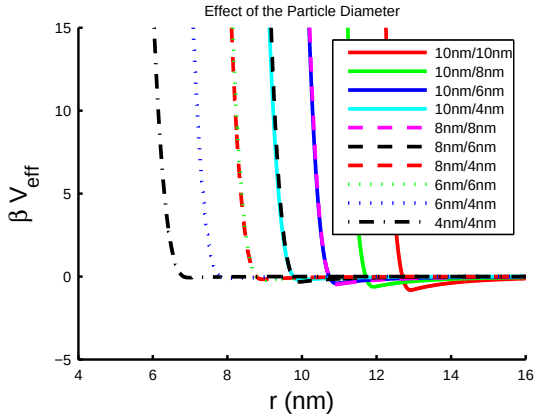

FIG. S8: Effective interaction between a semiconductor and a gold nanoparticle for particle diameters as labelled and with Hamaker constant $A = \sqrt{0.3 * 3.0}$ eV, capping layer thickness $L = 1.5$ nm, and ligand distance $s = 0.43$ nm at temperature $T = 300$ K.

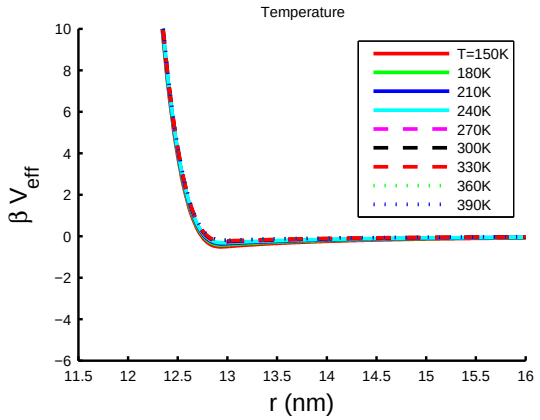

FIG. S9: Effective interactions between two 10 nm semiconductor nanoparticles for temperatures as labelled and with Hamaker constant $A = 0.3$ eV, capping layer thickness $L = 1.5$ nm, and ligand distance $s = 0.43$ nm.

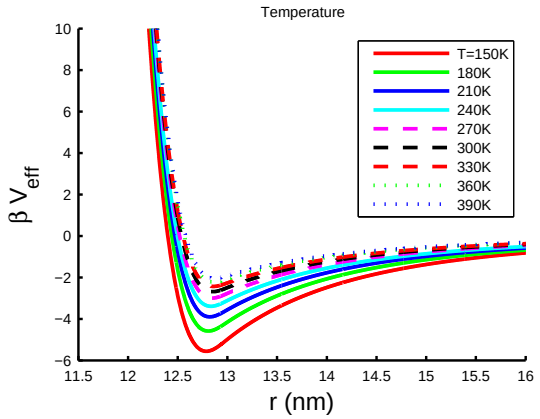

FIG. S10: Effective interactions between two 10 nm gold nanopaticles for temperatures as labelled with Hamaker constant $A = 3$ eV, capping layer thickness $L = 1.5$ nm, and ligand distance $s = 0.43$ nm.

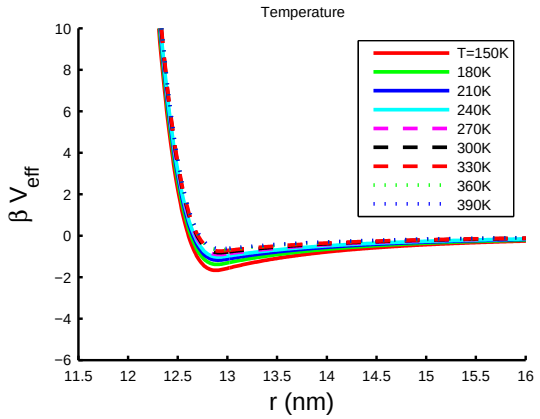

FIG. S11: Effective interactions between a semiconductor and a gold nanoparticle both with diameter 10 nm for temperatures as labelled and with Hamaker constant $A = \sqrt{0.3 * 3}$ eV, capping layer thickness $L = 1.5$ nm, and ligand distance $s = 0.43$ nm.

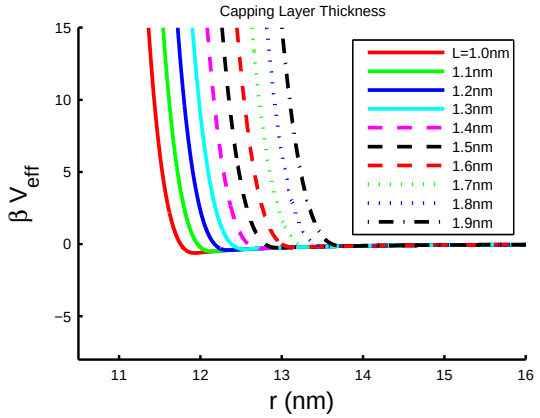

FIG. S12: Effective interactions between two 10 nm semiconductor nanoparticles for capping layer thicknesses L as labelled and with Hamaker constant $A = 0.3$ eV, and ligand distance $s = 0.43$ nm at temperature $T = 300$ K.

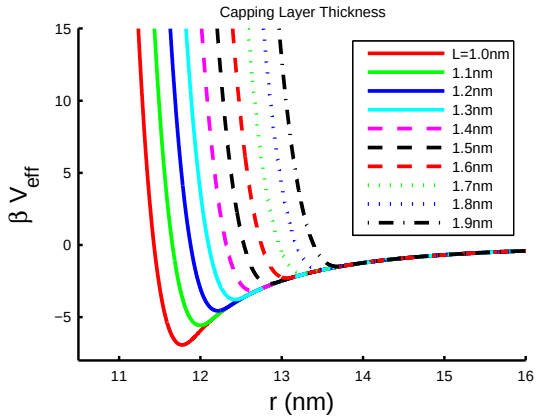

FIG. S13: Effective interactions between two 10 nm gold nanoparticles for capping layer thicknesses L as labelled and with Hamaker constant $A = 3$ eV, and ligand distance $s = 0.43$ nm at temperature $T = 300$ K.

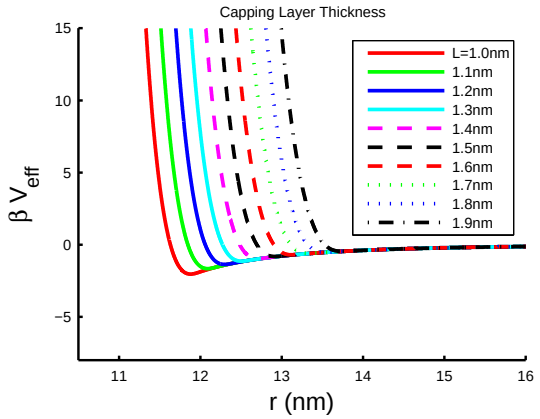

FIG. S14: Effective interactions between a 10 nm semiconductor nanoparticle and a 10nm gold nanoparticle for capping layer thicknesses L as labelled with Hamaker constant $A = \sqrt{3 * 0.3}$ eV, and ligand distance $s = 0.43$ nm at temperature $T = 300$ K.

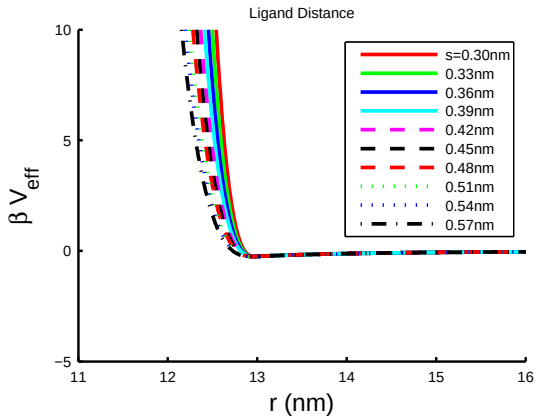

FIG. S15: Effective interactions between two 10 nm semiconductor nanoparticles for capping layer densities s as labelled with Hamaker constant $A = 0.3$ eV, and capping layer thickness $L = 1.5$ nm at temperature $T = 300$ K.

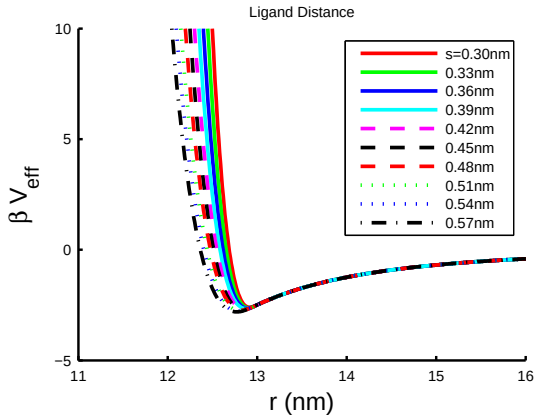

FIG. S16: Effective interactions between two 10 nm gold nanoparticles for capping layer densities s as labelled with Hamaker constant $A = 3$ eV, and capping layer thickness $L = 1.5$ nm at temperature $T = 300$ K

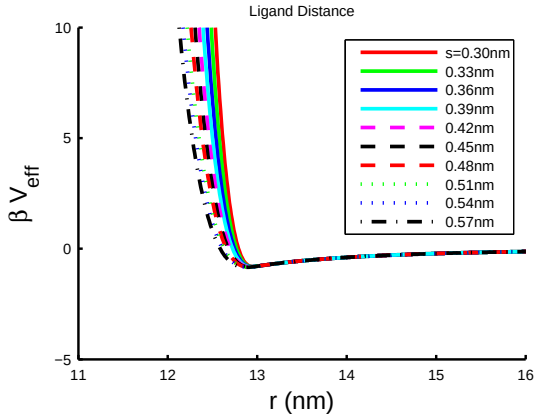

FIG. S17: Effective interactions between a 10 nm semiconductor nanoparticle and a 10 nm gold nanoparticle for capping layer densities s as labelled with Hamaker constant $A = \sqrt{3 * 0.3}$ eV, and capping layer thickness $L = 1.5$ nm at temperature $T = 300$ K.

[1] M. Dijkstra, R. van Roij, and R. Evans, Phys. Rev. E **59**, 5744 (1999).
[2] E. Trizac, M. D. Eldridge, and P. A. Madden, Mol. Phys. **90**, 675 (1997).
[3] M. D. Eldridge, P. A. Madden, P. N. Pusey, and P. Bartlett, Mol. Phys. **84**, 395 (1995).
[4] M. D. Eldridge, P. A. Madden, and D. Frenkel, Nature **365**, 35 (1993).
[5] A. Hynninen, L. Filion, and M. Dijkstra, J. Chem. Phys. **131**, 064902 (2009).
[6] W. Kranendonk and D. Frenkel, Mol. Phys. **72**, 679 (1991).
[7] D. Frenkel and B. Smit, *Understanding Molecular Simulation: From Algorithms to Applications* (Academic Press, San Diego, 1996).
[8] J. M. Polson, E. Trizac, S. Pronk, and D. Frenkel, J. Chem. Phys **112**, 5339 (2000).
[9] R. J. Speedy, J Phys. Cond. Mat. **10**, 4387 (1998).
[10] B. Derjaguin and L. Landau, Acta Physicochim. URSS **14**, 633 (1941).
[11] E. J. W. Verwey and J. T. Overbeek, *Theory of the stability of lyophobic colloids* (Elsevier, Amsterdam, 1948).
[12] C. N. Likos, Physics Reports **348**, 267 (2001).
[13] E. V. Shevchenko, D. V. Talapin, C. B. Murray, and S. O'Brien, J. Am. Chem. Soc. **128**, 3620 (2006).
[14] P. C. Ohara, D. V. Leff, J. R. Heath, and W. M. Gelbart, Phys. Rev. Lett **75**, 3466 (1995).
[15] J. Israelachvili, *Intermolecular and Surface Forces* (Academic Press, London, 1992).
[16] P. S. Shah, J. D. Holmes, K. P. Johnston, and B. A. Korgel, J. Phys. Chem. B **106**, 2545 (2002).
[17] A. E. Saunders and B. A. Korgel, J. Phys. Chem. B **108**, 16732 (2004).
[18] D. Bargeman and F. van Voorst Vader, J. Electroanal. Chem. **37**, 45 (1972).
[19] G. Ge and L. Brus, J. Phys. Chem. B **104**, 9573 (2000).
[20] B. A. Korgel, S. Fullam, S. Connolly, and D. Fitzmaurice, J. Phys. Chem. B **102**, 8379 (1998).